Particle dynamics in self-generated dunes over a range of hydraulic and sediment transport conditions using LES–DEM

Rui Sun[a], Heng Xiao[a,*], Kyle Strom[b]

[a]*Department of Aerospace and Ocean Engineering, Virginia Tech, Blacksburg, Virginia, USA*
[b]*Department of Civil and Environmental Engineering, Virginia Tech, Blacksburg, Virginia, USA.*

arXiv:1610.03397v1 [physics.geo-ph] 11 Oct 2016

Abstract

Direct measurement of vertical and longitudinal sediment fluxes on migrating sandy bedforms are extremely difficult to perform in both the field and laboratory. In this study we use the LES–DEM (large eddy simulation–discrete element method) solver *SediFoam* to examine the individual particle motions and resulting fluxes in a domain of self-generated dunes. In *SediFoam*, the motions of, and collisions among, the sediment grains as well as their interactions with surrounding turbulent flows are resolved. The numerical simulations are performed over a range of transport settings, spanning bedform inception through washout conditions, to examine the individual particle dynamics. The space-time evolution of dune surfaces is demonstrated. The self-generated dunes are stable at relatively low Reynolds numbers, but then become increasingly unstable at higher Reynolds numbers; eventually washing out as the number of bypass grains and particles in suspension increase. Data from the simulation are used to examine the vertical entrainment rate of particles and the fractionation of total sediment load into bed and suspended fractions as a function of transport conditions. The study also compares the sediment transport rate obtained using the bedform geometry and celerity to the true transport rate at different transport stages.

Keywords: particle dynamics, ripples, dunes, sediment transport, Large Eddy Simulation–Discrete Element Method

1. Introduction

The development of asymmetric bedforms at the interface of a flowing river and its bed is a distinguishing feature of sand-bed rivers. These features arise naturally as dynamically stable

*Corresponding author. Tel: +1 540 231 0926
Email addresses: sunrui@vt.edu (Rui Sun), hengxiao@vt.edu (Heng Xiao), strom@vt.edu (Kyle Strom)

entities birthed from instabilities in the coupled fluid and sediment system, and their presence strongly influences river hydraulic and sediment transport characteristics. Due to the importance of dunes in river mechanics, and their compelling physical and mathematical ascetics, their study has garnered substantial attention from researchers over many years (e.g., *Gilbert*, 1914; *Anderson*, 1953; *Kennedy*, 1963; *Mohrig and Smith*, 1996; *McElroy and Mohrig*, 2009; *Charru et al.*, 2013). Nevertheless, there is still much about dunes we are currently learning (e.g., *Naqshband et al.*, 2014; *Emadzadeh and Cheng*, 2016; *Venditti et al.*, 2016), and a unified quantitative approach to account for sediment mass flux in the longitudinal and vertical directions in the presence of migrating dunes is lacking (*García*, 2008).

Classic modeling of sediment transport in sand bed rivers conceptually discretizes active river beds into three vertical layers based on particle mobility and mode of transport (Fig. 1). These three layers consist of a stable bed layer (with particle velocities, $u_p = 0$, and solids volume fraction, or volume concentration, ε_s, greater than 0.5, and a vertical coordinate $y < y_o$), a mobile, but dense, bed load layer with variable thickness, δ_s, ($y_o \leq y \leq \eta$), and a more disperse suspended phase ($y > \eta$); based on this particular definition, the elevation of the bed surface, η, is taken to coincide with the top of the bed load layer. Under this conceptualization, the unit width volume flow rate of sediment traveling between $y = y_o$ and $y = \eta$ is the bed load transport rate, q_b $[L^2t^{-1}]$, and the volume flow rate of sediment moving in the longitudinal, x, direction above the elevation of $y = \eta$ is the suspended load, q_s $[L^2t^{-1}]$; the summation of the bed and suspended loads is the total load, q_t. Exchange between the bed and bed load layer is accounted for with the entrainment and deposition rates evaluated at $y = y_o$, $q_{e|o}$ and $q_{d|o}$. Similarly exchange between the bed load and suspended layers is accounted for using erosion and deposition functions evaluated at $y = \eta$, $q_{e|\eta}$ and $q_{d|\eta}$ (Fig. 1).

In typical reach-scale sediment transport calculations and morphodynamic simulations, the individual sediment particles are not directly resolved; nor are, in most cases, ripple or dune-scale changes in the bed elevation. Instead, sediment is modeled as a continuous substance, and moved throughout the domain using the vertical exchange terms, the computed fluid velocities, and the longitudinal bed or total loads. Common assumptions are that material in suspension travels with a speed equal to the fluid velocity; the bed load is in equilibrium with local conditions; and that $q_{d|\eta}$ and $q_{e|\eta}$ can be modeled as: $q_{d|\eta} = w_s\varepsilon_{s|b}$ and $q_{e|\eta} = w_sE_s = w_s\varepsilon_{s|be}$, where w_s is the

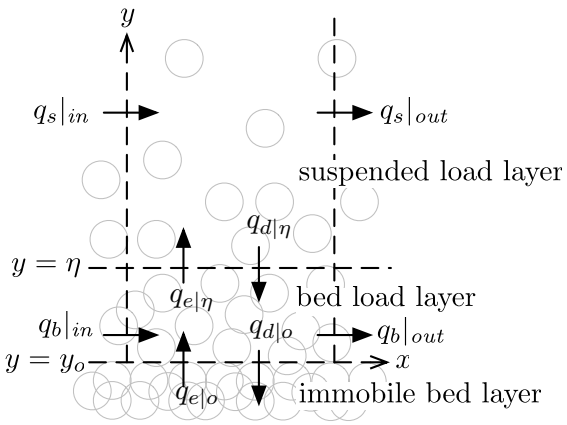

Figure 1: Sketch of the three-layer conceptualization of a mobile sediment bed.

terminal settling velocity of the sediment, $\varepsilon_{s|b}$ is sediment concentration near the interface of the suspended and bed load layer, and E_s (or $\varepsilon_{s|be}$) is the entrainment function, which is taken to be the near bed concentration under equilibrium conditions when erosion and deposition are locally balanced. Therefore, to model the movement of sediment and the resulting bed deformation, the closure equations for the sediment phase that are needed are the bed load flow rate, q_b, and the entrainment function, E_s.

Many empirical functions for these two quantities have been proposed over the years (*García*, 2008). However, obtaining data to evaluate q_b, q_s, and E_s independently and in detail is very difficult. Rather than measuring individual particle movements, sediment loads are measured in mass over some time interval and often only at one particular location along a stretch of river or laboratory flume. Furthermore, disentangling q_t, q_s, and q_b from experimental data, which typically consist of measurements of q_t and ε_s, can be difficult, and no direct measurements of E_s, that we are aware of, have been made in cases of actively migrating bedforms. Rather, reach averaged values of E_s are extracted from the vertical concentration profiles under equilibrium conditions (*Guy et al.*, 1966; *Garcia and Parker*, 1991).

When thinking about sand beds with migrating dunes, it is clear that spatial heterogeneities in the bed elevations will drive heterogeneities in the longitudinal and vertical turbulence properties of the flow and, hence, particle mobility (*Smith and McLean*, 1977; *van Rijn*, 1984b; *Best*, 2005). For example, the recent study of *Emadzadeh and Cheng* (2016) has highlighted that sediment entrainment rates vary at different spatial locations over fixed idealized dunes. While most sediment

transport calculations do not resolve bedform scale features, it is possible that further insights into the mechanics associated with actively migrating ripples and dunes in turbulent flows may come from a better understanding of particle motion over the bedform. In addition, the translation of these mechanics to sediment transport models such as those for q_b and E_s, could potentially be enhanced by examining the details of individual particle motions.

For example, advances have recently been made in understanding bed load transport in gravel beds using particle statistics obtained from high-speed cameras (*Ancey*, 2010; *Lajeunesse et al.*, 2010; *Roseberry et al.*, 2012; *Campagnol et al.*, 2015; *Fathel et al.*, 2015). Concurrent with this new data has been a drive to better describe the motion of the discrete sediment phase in terms of continuous river properties that can be used in larger-scale morphodynamic modeling (*Parker et al.*, 2000; *Ancey*, 2010; *Lajeunesse et al.*, 2010; *Furbish et al.*, 2012, 2016). The focus of these recent studies has been on the more sporadic motion of gravel particles traveling over a plane flume bed under equilibrium transport conditions with steady, uniform time-averaged hydraulics. Such conditions are different from those producing actively migrating sandy bedforms, but it is likely that some of the basic methodology and discussion generated by this body of work could also help to improve understanding of transport in sand bed rivers.

Examining particle motion in the presence of translating sandy bedforms presents at least two complications. The first is that steady hydraulics can only be obtained within a frame of reference that translates with the bedform. Secondly, even within a moving frame of reference, both vertical and longitudinal variation in the fluid and transport characteristics exists – even in the time averaged quantities (*Kostaschuk et al.*, 2009; *Naqshband et al.*, 2014). Furthermore, operations such as tracking the jump length of sand grains in experimental ripples and dunes is difficult. This is due to the combination of particle sizes smaller than gravels, travel distances that can be up to and longer than one bedform wavelength, large numbers of nearly identical particles in motion, and opaque water. Needless to say, such constraints exceed the limits that even the state of the art imaging and image processing technology can currently achieve.

A secondary approach to bolstering our understanding of particle motion in beds with actively migrating bedforms, is to make use of interface-resolved direct numerical simulations, which resolve both the turbulent flow, the flow field surrounding each particle, and the interparticle collisions (*Aussillous et al.*, 2013; *Fukuoka et al.*, 2014; *Kidanemariam and Uhlmann*, 2014). Such

methods have proved especially fruitful in painting a better picture of the interplay between turbulence and sediment transport over plane beds (e.g., *Kempe et al.*, 2014; *Vowinckel et al.*, 2014). A drawback to such methods, however, is that they are highly expensive computationally. For example, the computational cost for sediment transport simulation of 27,000 grains on a flat bed is 30 million CPU hours (*Vowinckel et al.*, 2014). Because of the expense, most simulations have focused on active sediment transport in the absence of self-generated bedforms; an exception to this statement is the study of *Kidanemariam and Uhlmann* (2014).

In the past few years researchers started to use modern, general-purpose particle-resolving solvers based on LES–DEM to study sediment transport. The LES–DEM has been used extensively in the past two decades in the chemical and pharmaceutical industry on a wide range of applications such as fluidized beds, cyclone separator, and pneumatic conveying (*Han et al.*, 2003; *Ebrahimi*, 2014). In LES–DEM, Large eddy simulation is used to model the fluid flow, which is coupled with the discrete element method for resolving particle motions. In his pioneering work, *Schmeeckle* (2014) used an open-source LES–DEM solver (*Goniva et al.*, 2009; *Kloss et al.*, 2012) to study suspended sediment transport over featureless beds. The LES–DEM approach is also proved to be capable of simulating the self-generated dunes in a pipe or channel (*Arolla and Desjardins*, 2015; *Sun and Xiao*, 2016a).

It has recently been shown that *SediFoam*, a hybrid LES–DEM solver for particle-laden flows (*Sun and Xiao*, 2016b), is capable of producing self-organized bedforms with characteristic height and migration celerities similar to those observed in laboratory flumes (*Sun and Xiao*, 2016a). In this study, we use *SediFoam* to examine the individual particle dynamics of sand grains in a field of self-organize asymmetric ripples. This is done over a range of transport settings, spanning from bedform inception to washout conditions. The particle velocities are then temporally and spatially averaged in a moving frame of reference to extract key sediment transport quantities. The averaged values are then compared to empirical formulas used in one-dimensional river morphodynamic modeling, with the primary intent of showing that DEM approaches can be used to extract the types of data needed to improve understanding and modeling in cases of actively migrating sandy bedforms. Examining these properties in a moving frame of reference also allows us to examine the link between translation and deformation of ripples/dunes in light of spatially varying bed and suspended loads.

2. Methodology

SediFoam is an open-source, highly parallel, robust LES–DEM solver with emphasis on sediment transport applications. It is capable of simulating the interaction between turbulent structures and sediment particles. The modeling of translational and rotational motion of each sediment particle is based on Newton's second law as the following equations (*Cundall and Strack*, 1979):

$$m\frac{d\mathbf{u}_p}{dt} = \mathbf{f}^{col} + \mathbf{f}^{fp} + m\mathbf{g}, \tag{1a}$$

$$I\frac{d\mathbf{\Psi}_p}{dt} = \mathbf{T}^{col} + \mathbf{T}^{fp}, \tag{1b}$$

where m is the mass of particle; $\mathbf{u}_p$ is particle velocity; t is time; $\mathbf{f}^{col}$, $\mathbf{f}^{fp}$ are particle–particle collision force and fluid–particle interaction force, respectively; $\mathbf{g}$ denotes gravity. Similarly, I and $\mathbf{\Psi}_p$ are angular moment of inertia and angular velocity of the particle; $\mathbf{T}^{col}$ and $\mathbf{T}^{fp}$ are the torques due to inter-particle contact and fluid–particle interaction, respectively. Note that the vectors and tensors are denoted using boldface letters (e.g., $\mathbf{u}$). To compute the collision forces and torques, the particles are modeled as soft spheres with inter-particle contact represented by an elastic spring and a viscous dashpot. Further details can be found in *Tsuji et al.* (1993).

Locally-averaged incompressible Navier–Stokes equations are used to describe the fluid flow. Assuming constant fluid density ρ_f, the governing equations for the fluid are (*Anderson and Jackson*, 1967; *Kafui et al.*, 2002):

$$\nabla \cdot (\varepsilon_s \mathbf{U}_s + \varepsilon_f \mathbf{U}_f) = 0, \tag{2a}$$

$$\frac{\partial (\varepsilon_f \mathbf{U}_f)}{\partial t} + \nabla \cdot (\varepsilon_f \mathbf{U}_f \mathbf{U}_f) = \frac{1}{\rho_f}\left(-\nabla p + \varepsilon_f \nabla \cdot \tau + \varepsilon_f \rho_f \mathbf{g} + \mathbf{F}^{fp}\right), \tag{2b}$$

where ε_s is the solid volume fraction; $\varepsilon_f = 1 - \varepsilon_s$ is the fluid volume fraction; $\mathbf{U}_f$ is the fluid velocity. The terms on the right hand side of the momentum equation are: pressure gradient ∇p, divergence of the stress tensor τ (including viscous and Reynolds stresses), gravity, and fluid–particle interaction forces per unit mass, respectively. In the present study, large-eddy simulation is applied to resolve the flow turbulence. The stress tensor is composed of both viscous and Reynolds stresses: $\tau = \mu \nabla \mathbf{U}_f + \rho_f \mathcal{R}$, where μ is the molecular viscosity of fluid and $\mathcal{R}$ is the Reynolds stress. The expression of the Reynolds stress is:

$$\mathcal{R} = \frac{2}{\rho_f}\mu_t \mathbf{S} - \frac{2}{3}k\mathbf{I}, \tag{3}$$

where μ_t is the eddy viscosity, $\mathbf{S} = (\nabla \mathbf{U}_f + (\nabla \mathbf{U}_f)^T)/2$ is the rate-of-strain tensor, k is the turbulent kinetic energy, and I is the identity matrix. We applied the one-equation eddy viscosity model proposed by *Yoshizawa and Horiuti* (1985) as the sub-grid scale (SGS) model. This model is selected because of its capability of simulating turbulent flow in a periodic channel (*Horiuti*, 1985). It is noted that in the stress tensor τ term, the fluctuations of the fluid flow at the boundary of the particle are not resolved. The Eulerian fields ε_s, $\mathbf{U}_s$, and $\mathbf{F}^{fp}$ in Eq. (2) are obtained by averaging the information of Lagrangian particles.

The fluid-particle interaction force $\mathbf{f}^{fp}$ consists of buoyancy $\mathbf{f}^{buoy}$, drag $\mathbf{f}^{drag}$, lift force $\mathbf{f}^{lift}$. The drag force model proposed by *Syamlal et al.* (1993) is applied to the present simulations. The drag on an individual component sphere i is formulated as:

$$\mathbf{f}_i^{drag} = \frac{V_{p,i}}{\varepsilon_{f,i}\varepsilon_{s,i}} \beta_i \left(\mathbf{u}_{p,i} - \mathbf{U}_{f,i}\right), \tag{4}$$

where $V_{p,i}$ and $\mathbf{u}_{p,i}$ are the volume and the velocity of particle i, respectively; $\mathbf{U}_{f,i}$, $\varepsilon_{f,i}$, and $\varepsilon_{f,i}$ are the fluid velocity, solid volume fraction, and fluid volume fraction interpolated to the center of particle i, respectively; β_i is the drag correlation coefficient which accounts for the presence of other particles. The β_i value in the present study is based on *Syamlal et al.* (1993):

$$\beta_i = \frac{3}{4}\frac{C_{d,i}}{V_{r,i}^2}\frac{\rho_f |\mathbf{u_{p,i}} - \mathbf{U_{f,i}}|}{d_{p,i}}, \quad \text{with} \quad C_{d,i} = \left(0.63 + 0.48\sqrt{V_{r,i}/\mathrm{Re_{pv,i}}}\right), \tag{5}$$

where $C_{d,i}$ is the drag coefficient of particle i; $d_{p,i}$ is the diameter of particle i; the particle velocity Reynolds number $\mathrm{Re_{pv,i}}$ is defined as:

$$\mathrm{Re_{pv,i}} = \rho_s d_{p,i} |\mathbf{u_{p,i}} - \mathbf{U_{f,i}}|; \tag{6}$$

the $V_{r,i}$ is the correlation term for the i-th particle:

$$V_{r,i} = 0.5\left(A_{1,i} - 0.06\mathrm{Re_{pv,i}} + \sqrt{(0.06\mathrm{Re_{pv,i}})^2 + 0.12\mathrm{Re_{pv,i}}(2A_{2,i} - A_{1,i}) + A_{1,i}^2}\right), \tag{7}$$

with

$$A_{1,i} = \varepsilon_{f,i}^{4.14}, \quad A_{2,i} = \begin{cases} 0.8\varepsilon_{f,i}^{1.28} & \text{if } \varepsilon_{f,i} \le 0.85, \\ \varepsilon_{f,i}^{2.65} & \text{if } \varepsilon_{f,i} > 0.85. \end{cases} \tag{8}$$

In addition to drag, the lift force on a spherical component particle is modeled as (*Saffman*, 1965; *van Rijn*, 1984a; *Zhu et al.*, 2007):

$$\mathbf{f}_i^{lift} = C_l(\rho_f \mu)^{0.5} d_{p,i}^2 \left(\mathbf{U}_{f,i} - \mathbf{u}_{p,i}\right) \times \frac{\omega_i}{|\omega_i|^{0.5}}, \tag{9}$$

where $C_l = 1.6$ is the lift coefficient, $\omega_i = \nabla \times \mathbf{U}_{f,i}$ is the curl of flow velocity interpolated to the center of particle i, and $\times$ indicates the cross product between vectors.

3. Implementations and Numerical Methods

The hybrid LES–DEM solver *SediFoam* is developed based on two state-of-the-art open-source codes in their respective fields. LES is performed by using CFD (Computational Fluid Dynamics) toolbox OpenFOAM (Open Field Operation and Manipulation)(*OpenCFD*, 2013), and DEM is performed by a molecular dynamics simulator LAMMPS (Large-scale Atomic/Molecular Massively Parallel Simulator) which is developed at the Sandia National Laboratories (*Plimpton*, 1995). A parallel LAMMPS–OpenFOAM interface is implemented for the communication of the two open-source solvers. The code is publicly available at https://github.com/xiaoh/sediFoam under GPL license. Detailed introduction of the implementations of this hybrid solver is discussed in *Sun and Xiao* (2016b).

The fluid equations in (2) are solved in OpenFOAM with the finite volume method (*Jasak*, 1996). PISO (Pressure Implicit Splitting Operation) algorithm is used to prevent velocity–pressure decoupling (*Issa*, 1986). A second-order central scheme is used for the spatial discretization of convection and diffusion terms. Time integrations are performed with a second-order implicit scheme. An averaging algorithm based on diffusion is implemented to obtain smooth ε_s, $\mathbf{U}_s$ and $\mathbf{F}^{fp}$ fields from discrete sediment particles (*Sun and Xiao*, 2015a,b). In the averaging procedure, the diffusion equations are solved on the same mesh for LES. A second-order central scheme is used for the spatial discretization of the diffusion equation; a second-order implicit scheme is used for the temporal integration. To resolve the collision between the sediment particles, the contact force between sediment particles is computed with a linear spring-dashpot model (*Cundall and Strack*, 1979). The time step to resolve the particle collision is less than 1/50 the contact time to avoid particle inter-penetration (*Sun et al.*, 2007).

4. Conditions for runs

The numerical tests of the self-generated bedforms are performed at different bulk Reynolds numbers $\mathrm{Re_b}$ varying from 6,000 to 12,000. The setup of the numerical tests is based on previous studies of bedform migration (*Kidanemariam and Uhlmann*, 2014; *Sun and Xiao*, 2016a). The

dimensions of the domain, the mesh resolutions, and the fluid and particle properties are detailed in Table 1. The geometry of the domain is shown in Fig. 2, and x-, y- and z- coordinates are aligned with the streamwise, wall-normal, and lateral directions, respectively. The LES mesh in streamwise (x-) and lateral (z-) directions is uniform in size; whereas the grid segments in vertical (y-) direction are progressively refined towards the bottom boundary. The boundary conditions for both pressure field and velocity field are periodic in both x- and z-directions. In y-direction, zero-gradient boundary condition is applied for pressure field; no-slip wall condition is applied at the bottom for velocity field, and slip wall condition is applied on the top. To provide a bottom boundary condition for the moving particles, three layers of fixed particles are arranged hexagonally at the bottom. A perturbation of the first layer of the fixed particles is added to avoid moving particles from forming perfect lattice. This is because the perfect lattice of sediment particles can significantly reduce the sediment transport rate.

The initialization of the present numerical simulations follows previous studies (*Kidanemariam and Uhlmann*, 2014; *Sun and Xiao*, 2016a). A separate simulation of particle settling without considering the hydrodynamic forces is performed to obtain an initial configuration of the particles. In this settling simulation, particles fall from random positions under gravity with inter-particle collisions. To initialize the fluid flow, each simulation first runs 20 flow-through times with all particles fixed at the bottom.

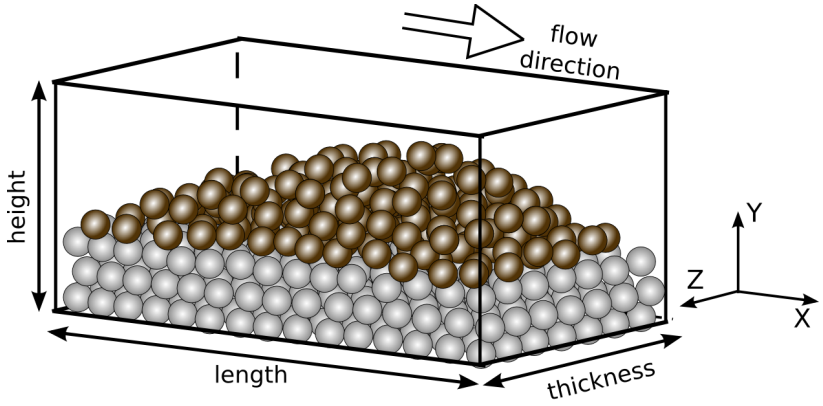

Figure 2: Layout of the numerical simulations of self-generated dunes. The brown particles are moving particles; the gray particles are fixed to provide rough wall boundary conditions. Note that the particle and dune sizes are not to scale.

Table 1: Parameters of the numerical simulations.

	Case 1	Case 2	Case 3	Case 4
Domain dimensions				
width, height, thickness (L_x/d_p, L_y/d_p, L_z/d_p)		$312 \times 33 \times 80$		
Mesh resolutions				
width, height, thickness (N_x, N_y, N_z)		$120 \times 140 \times 40$		
Particle properties				
total number		272,000		
diameter d_p [mm]		0.5		
density ρ_s [$\times 10^3$ kg/m^3]		2.5		
terminal settling velocity w_s [m/s]		0.06		
particle stiffness coefficient [N/m]		200		
normal restitution coefficient		0.3		
coefficient of friction		0.4		
Fluid properties and flow conditions				
kinetic viscosity ν [$\times 10^{-6}$ m^2/s]		1.5		
density ρ_f [$\times 10^3$ kg/m^3]		1.0		
bulk Reynolds number $\mathrm{Re_b} = U_b H_b/\nu$	6,000	8,000	10,000	12,000
mean flow velocity U_b [m/s]	0.39	0.52	0.65	0.78

5. Results

5.1. Shear velocity decomposition and averaged transport conditions

The simulation conditions listed in Table 1 gave rise to the development of mobile bedforms. Because of this, the pressure gradient needed to maintain the unit width discharge of water had to increase from the initial value within each simulation as more and more particles began to move, collide, and self-organize into bedforms. As will be discussed in the next section, bedforms grew in size from Case 1 to Case 2, and then began to wash out in Cases 3 and 4. As such, the total boundary resistance increased from Case 1 to 2, decreased from Case 2 to 3, and then increased again between Cases 3 and 4. This up and down behavior in the total resistance occurred even though the fluid discharge and velocity monotonically increased with each case or Reynolds number.

To make the results of the simulations more comparable to classic sediment transport theory, we decomposed the total shear shear stress τ into a frictional component τ' and the bedform and collision-drag component τ'' with $\tau = \tau' + \tau''$. The frictional component, τ', was calculated from the force needed to drive the flow at the given flow rate before significant particle motion or bedform development. This is the friction between the water and the bed at the sediment grain size scale. In contrast, the total shear stress τ values were obtained from the average of the total force needed to sustain the unit width discharge once the bedforms had fully developed. The contributions from the form drag and the collisions between suspended and the immobile particles were then inferred by taking the difference between the two, i.e., $\tau'' = \tau - \tau'$. Finally, following the conventions in sediment transport literature, we use the corresponding friction velocities defined as $u_* = \sqrt{\tau/\rho_f}$, $u'_* = \sqrt{\tau'/\rho_f}$ and $u''_* = \sqrt{\tau''/\rho_f}$, respectively, to denote the three shear stress components. Shear velocity values for these three components are given in Table 2 along with key contextual sediment transport parameters, all of which were calculated using the friction shear stress u'_*.

5.2. Bed form morphology and evolution

The bedform morphology and evolution obtained from numerical simulations of various bulk Reynolds numbers are compared in this section. In our previous study (*Sun and Xiao*, 2016a), we had already demonstrated that the LES–DEM model is capable of self-generating bedforms with physically meaningful heights, wavelengths, and migration velocities. The simulated characteristics had been validated against experimental measurements and interface-resolved simulations reported

Table 2: Resulting shear velocities, sediment transport conditions, and bedform features at different bulk Reynolds numbers $\mathrm{Re_b}$. All transport conditions are calculated with the skin friction shear velocity, u'_*. Bed form characteristics were given for $t^* \in [700, 750]$.

	Case 1	Case 2	Case 3	Case 4
Shear velocity decomposition				
total shear velocity u_* [m/s]	0.037	0.081	0.072	0.088
fluid friction shear velocity u'_* [m/s]	0.032	0.045	0.057	0.069
collisional and form shear velocity u''_* [m/s]	0.019	0.067	0.043	0.055
ratio of collisional/form drag to total, u''^2_*/u^2_*	0.25	0.69	0.37	0.39
Sediment transport conditions				
particle Reynolds number $\mathrm{Re_p} = d_p\sqrt{gR_sd_p}/\nu$		43		
critical Shields parameter θ_{cr}		0.032		
Shields parameter θ	0.15	0.28	0.44	0.65
w_s/u'_*	1.88	1.33	1.05	0.87
Shields parameter θ	0.15	0.28	0.44	0.65
mobility condition θ/θ_{cr}	4.6	8.5	13.6	20.0
total load $q^*_t = q_t/d_p\sqrt{gR_sd_p}$	0.04	1.12	0.97	4.65
suspended load fraction, $\alpha_s = q^*_s/q^*_t$	0.05	0.54	0.56	0.74
Bed form characteristics				
wavelength (L_d/d_p)	160	312	312 [(a)]	N.A.
height (H_d/d_p)	3.1	11.6	7.2 [(a)]	N.A.
migration velocity (U_d/U_b)	0.017	0.053	0.088 [(a)]	N.A.
bed form transport rate $q^*_{bf} = q_{bf}/d_p\sqrt{gR_sd_p}$	0.06	0.93	N.A.	N.A.

Note: (a) While bedform characteristics are presented for Case 3, it should be noted that any structure that was present at a given time was highly unstable and significantly less dune-like than the bedforms in Cases 1 and 2.

in the literature (*Kidanemariam and Uhlmann*, 2014). The bedforms that develop in the present study are similar. Based on the calculated Shields parameter, $\theta = 0.15$ to 0.65, and a particle Reynolds number of $\mathrm{Re_p} = d_p\sqrt{gR_s d_p}/\nu = 43$ (Table 1), where $R_s = (\rho_s - \rho)/\rho$ is the submerged specific gravity. We can say that the simulation conditions are inline with those that should give rise to bed load dunes that transition to suspension dominated dunes according to the Shields-Parker river sedimentation diagram (*García et al.*, 2000). In accordance with this, we will refer to the bedforms developed in the simulation as "dunes" even though the absolute heights of the bedforms are rather small.

The space-time evolutions of the dune surface at various bulk Reynolds numbers are plotted in gray scale in Fig. 3. This aims to demonstrate the variation of the dune surface in the temporal and spatial domain. The surface of the dune is determined by using a threshold value $\varepsilon_s = 0.1$ according to *Kidanemariam and Uhlmann* (2014). Dark and light oblique stripes, which are the peaks and troughs of the dunes respectively, can be observed at all Reynolds numbers. The bulk Reynolds number $\mathrm{Re_b}$ is defined as $U_b H_b/\nu$, where $H_b = 25d_p$ is the flow depth as measured from the initial bed surface to the top of the computational domain. Moreover, the dunes at all bulk Reynolds numbers are developed from the perturbations on the flat bed, which is consistent with the observations by *Kidanemariam and Uhlmann* (2014). To facilitate presentation, the physical time t is normalized by the constant $T = H_b/U_b$, and thus the resulting non-dimensional time is denoted as $t^* = t/T$. Figure 3(a) shows that the slope of the stripes after non-dimensional time $t^* > 400$ is smaller than that of $t^* \in [200, 400]$. The decrease of the slope indicates the dune migration velocity decreases due to the growth of the dune, which is also observed in previous experimental studies (*Ouriemi et al.*, 2009). Since flow rate q_f is constant and sediment transport rate does not vary significantly when the dunes are generated, larger dunes move slower (*Paarlberg et al.*, 2006). Comparing the slope of the stripes in each case (Fig. 3), one can observe that dune migration velocity increases with the Reynolds number or shear. This occurs even though the dunes grow in size from Case 1 to 2, indicating an overall increase in the sediment transport rate due to the faster moving particles and bed forms.

It can be also seen in Fig. 3 that the dune surfaces are stable in Cases 1 and 2, and unstable in Case 3 and 4. To further investigate the stability of the dune, the profiles of the dune surfaces obtained in each case during $t^* \in [600, 800]$ are plotted in Fig. 4. The time interval $t^* \in [600, 800]$

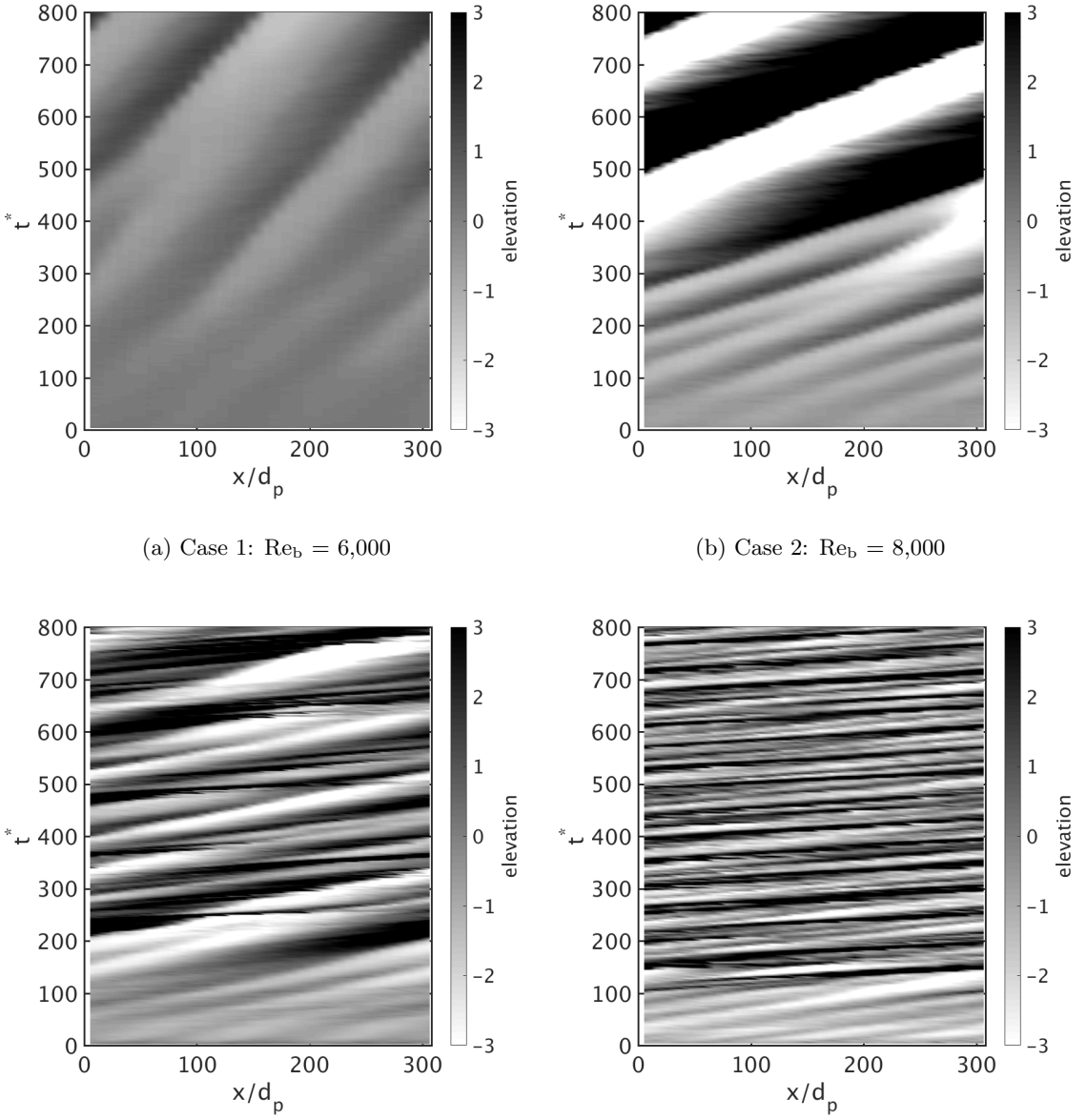

(a) Case 1: $\mathrm{Re_b}$ = 6,000

(b) Case 2: $\mathrm{Re_b}$ = 8,000

(c) Case 3: $\mathrm{Re_b}$ = 10,000

(d) Case 4: $\mathrm{Re_b}$ = 12,000

Figure 3: Time-space evolution of the dune at bulk Reynolds numbers $\mathrm{Re_b}$ from 6,000 to 12,000. The color of the contour indicates the height of the dune surface compared to the initial flat bed.

is selected because the dunes are developed during this time. The profiles of the dunes are plotted using the relative longitudinal location with respect to the dune, X, where $X = x - U_d t$, x is the fixed downstream direction, and U_d is the dune migration velocity. When the dune is stable, dune surface profiles are overlapping when plotted in the moving-frame. It can be seen in Figs. 4(a) and 4(b) that the self-generated dunes in Case 1 and 2 are stable and the dune surface profiles are highly overlapped. In contrast, the dune profiles in Fig. 4(c) are not overlapping, and there is an offset of about $50d_p$ between the time-averaged dune profiles obtained when $t^* \in [600, 650]$ and $t^* \in [700, 750]$. The offset between the dune profiles at different time intervals shows that the dune surface profile at bulk Reynolds number $\mathrm{Re_b} = 10{,}000$ (Case 3) is less stable than those at lower Reynolds numbers or shear. This suggests that the present simulation at $\mathrm{Re_b} = 10{,}000$ captures the transition from 'dune migration' to 'suspended sediment transport'. At even higher bulk Reynolds number $\mathrm{Re_b} = 12{,}000$, shown in Fig. 4(d), the time-averaged dune profiles when $t^* \in [600, 650]$ and $t^* \in [700, 750]$ fluctuate even more than those at $\mathrm{Re_b} = 10{,}000$. Although dunes are still generated at $\mathrm{Re_b} = 12{,}000$, they are very unstable because the shear stress of the fluid flow is high enough to wash out the dunes almost immediately after they appear.

To quantitatively compare the dune features at different bulk Reynolds numbers, the dune height H_d, the dune wavelength L_d, and the migration velocity U_d of the dunes obtained in the present simulations are summarized in Table 2. The height and wavelength of the dunes are obtained by averaging the dune surface profiles, and the dune migration velocity is obtained from the slope of the stripes in Fig. 4. Since the dunes generated at $\mathrm{Re_b} \geq 10,000$ are highly unstable, the dune features are obtained during $t^* \in [700, 750]$ when the dunes appear at all Reynolds numbers. When bulk Reynolds number increases from 6,000 to 8,000, the wavelength of the dune increases from $160d_p$ to $312d_p$, and the height of the dune grows from $3.1d_p$ to $11.6d_p$. This increase of the dune wavelength and height indicates the dune grows faster at higher Reynolds numbers, which is also observed in the experiments (*Ouriemi et al.*, 2009). This is attributed to the fact that the sediment transport rate increases significantly when the flow rate increases. As can be seen in Table 2, the dune height decreases when bulk Reynolds number increases from 8,000 to 12,000. Although the sediment transport rate still increases, particles begin to have longer jump length or move in suspension, resulting in a move towards dune washout. In addition, the increase of the non-dimensional dune migration velocity is observed in the present simulations. When the flow

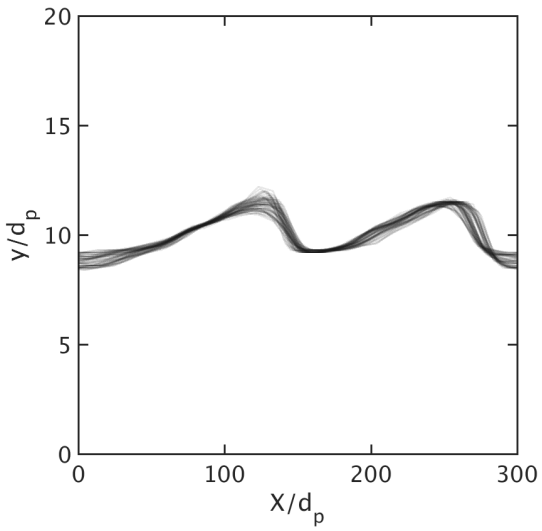

(a) Case 1: $\mathrm{Re_b} = 6{,}000$

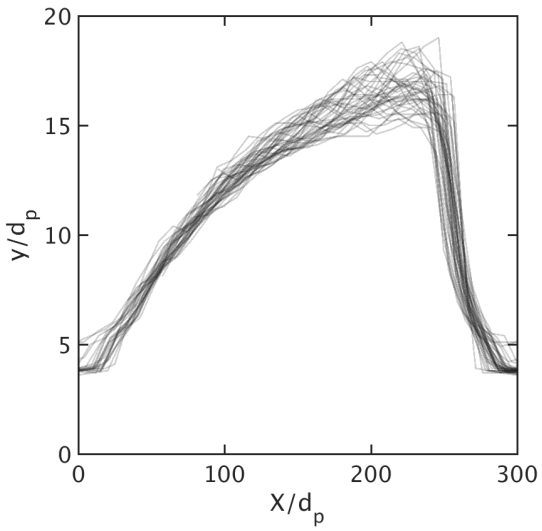

(b) Case 2: $\mathrm{Re_b} = 8{,}000$

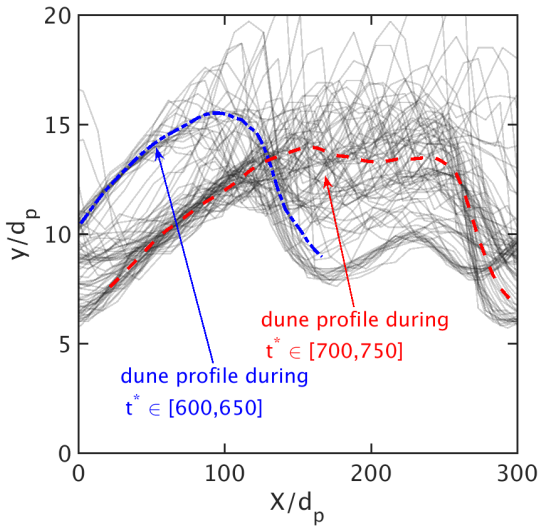

(c) Case 3: $\mathrm{Re_b} = 10{,}000$

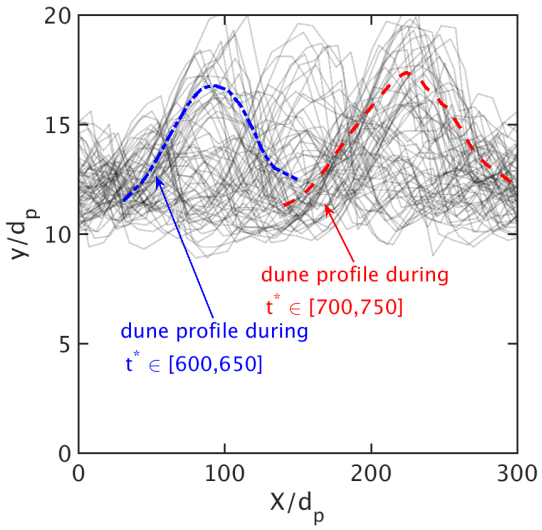

(d) Case 4: $\mathrm{Re_b} = 12{,}000$

Figure 4: The surface of the dune when $t^* \in [600, 800]$ at bulk Reynolds numbers $\mathrm{Re_b}$ from 6,000 to 12,000, where the non-dimensional time is defined as $t^* = tU_b/H_b$. The x-axis is the relative longitudinal location with respect to the dune, X, where $X = x - U_d t$, x is the fixed downstream direction, and U_d is the dune velocity.

velocity increases, the growth of sediment transport rate is much larger than the increase of flow velocity, and thus the non-dimensional dune migration increases.

5.3. Individual particle transport characteristics

A unique advantage of the LES–DEM approach over low-fidelity, continuum-scale simulation approaches is its capability to capture the trajectories of individual sediment particles. To fully utilize this advantage offered by the high-fidelity approach, we compare the trajectories of sediment particles when moving over the dune surface at different bulk Reynolds numbers. Our aim in plotting the trajectories of individual sediment particles is to demonstrate the variation of the particle behavior at different bulk Reynolds numbers and under different sediment transport regimes (i.e., bed load, mixed, and suspended load). In addition, the motion of the buried individual particles at bulk Reynolds number $\mathrm{Re_b}$ = 6,000 is presented. The study of the burial of the individual particles aims to investigate the trajectories of sediment particles during dune migration process.

The snapshots of the individual particles jumping over the dune at bulk Reynolds number $\mathrm{Re_b}$ = 6,000 during $t^* \in [700, 718]$ are shown in Fig. 5. To demonstrate the jumping process of the sediment particles, we randomly selected 20 particles with initial velocity $u_p > 0.1$ m/s on the stoss side and plotted their trajectories. The inverval between two consecutive snapshots is $\Delta t^* = 6$, or equivalently $\Delta t = 0.2$ s at $\mathrm{Re_b} = 6,000$. It can be seen in the figures that overall behavior of the selected particles on the dune surface is similar. On the stoss side, these selected particles gain energy from the fluid flow and move faster than the dune. However, on the lee side, the flow velocity decreases after the dune peak, and thus the deposition of the particles can be observed. Since the particles on the stoss side jump over the peak of the dune and deposit on the lee side, the dune progresses downstream.

The trajectories of individual particles at various bulk Reynolds numbers during $t^* = [700, 725]$ in the longitudinal jumping process are shown in Fig. 6, which is to demonstrate the variation of longitudinal jumping in different flow regimes. When the bulk Reynolds number increases from 6,000 to 8,000, the jumping length of the particles significantly increases. At $\mathrm{Re_b}$ = 8,000, both the bulk velocity and the height of the dune in the channel are larger than those at $\mathrm{Re_b}$ = 6,000, and thus the flow velocity on the stoss side of the dune increases. Therefore, the longitudinal jumping velocity of the individual particle in the flow and the jumping length also grow. However, at bulk

Reynolds number $\mathrm{Re_b}$ = 12,000, the dune is washed out and behavior of the selected particles is not associated with the surface of the bed.

The probability density functions of the particle jumping distances are plotted in Fig. 7. The jumping of sediment particles is determined by using U_d as threshold velocity. At bulk Reynolds number $\mathrm{Re_b}$ = 6,000, the peak of the probability density function is at $x/d_p = 30$, which is much smaller than the dune wavelength $x/d_p = 150$. This is because at $\mathrm{Re_b}$ = 6,000 the longitudinal jumping occurs when the particles are close to the peak of the dune. At this Reynolds number, the probability density of the particles jumping over $x/d_p = 150$ is small. This indicates the number of bypassed sediment particles is negligible and the wavelength $x/d_p = 150$ in this case is stable. At $\mathrm{Re_b}$ = 8,000, the peak of the probability density function moves to $x/d_p = 150$. When dune is generated in the channel, the flow field on the stoss side would be influenced by the dune and a vertical flow velocity can be observed (*Naqshband et al.*, 2014). Hence, the resident time of jumping particles is longer and the peak in the probability density function increases. At $\mathrm{Re_b}$ = 10,000, the peak of the probability density function is also at $x/d_p = 150$. Due to the increase of bulk flow velocity, the number of particles jumping over longer distances increases. When the Reynolds number continues to increase to 12,000, a small peak at $x/d_p = 100$ can be also observed. The magnitude of this peak is small because the dune formed at $\mathrm{Re_b}$ = 12,000 is very unstable. Moreover, the probability density of the jumping distance of $x/d_p > 300$ is significantly larger than those at smaller Reynolds numbers. Due to the increase of the probability density of long-jumping particles, the number of bypassed sediment particle is much larger and the suspended load is dominant at this Reynolds number.

The snapshots of the burial process of individual particles at bulk Reynolds number $\mathrm{Re_b}$ = 6,000 are demonstrated in Fig. 8. We selected 100 representative particles on the surface at $t_0^* = 700$ and highlighted them in red color. It can be seen in Fig. 8(a) that the highlighted particles are rolling and jumping on the dune surface at the initial time step. At $t_0^* + 40$, these highlighted particles are deposited on the same location ($x/d_p = 120$) at the lee side of the dune, which is shown in Fig. 8(b). Comparing from the locations of the highlighted particles in Fig. 8(b) and 8(c), when the particles are buried in the sediment bed, they do not move with the migration of the dune. This is because the buried particles are below the dune surface and the influence of fluid flow on them is negligible. When dune continues to move forward, shown in Fig. 8(d), some buried particles are

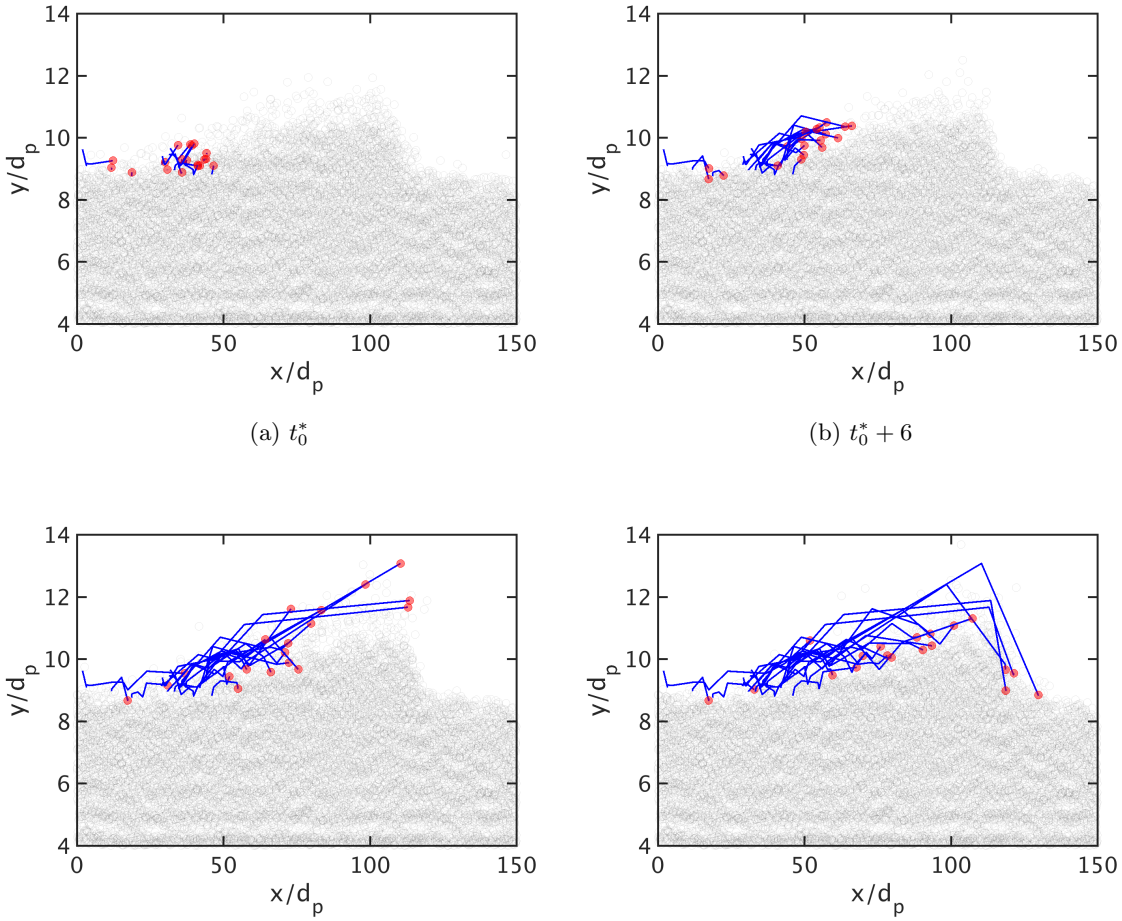

(a) t_0^* (b) $t_0^* + 6$

(c) $t_0^* + 12$ (d) $t_0^* + 18$

Figure 5: The trajectories of the sediment particles on the crest of the dune at bulk Reynolds number $\mathrm{Re_b} = 6{,}000$ starting from non-dimensional time $t_0^* = 700$. The time is normalized based on flow depth H_b and bulk velocity U_b as $t^* = tU_b/H_b$. Each circle represents a sphere particle: red circle are highlighted particles; gray particles are non-highlighted. Solid lines are the trajectories of the highlighted particles.

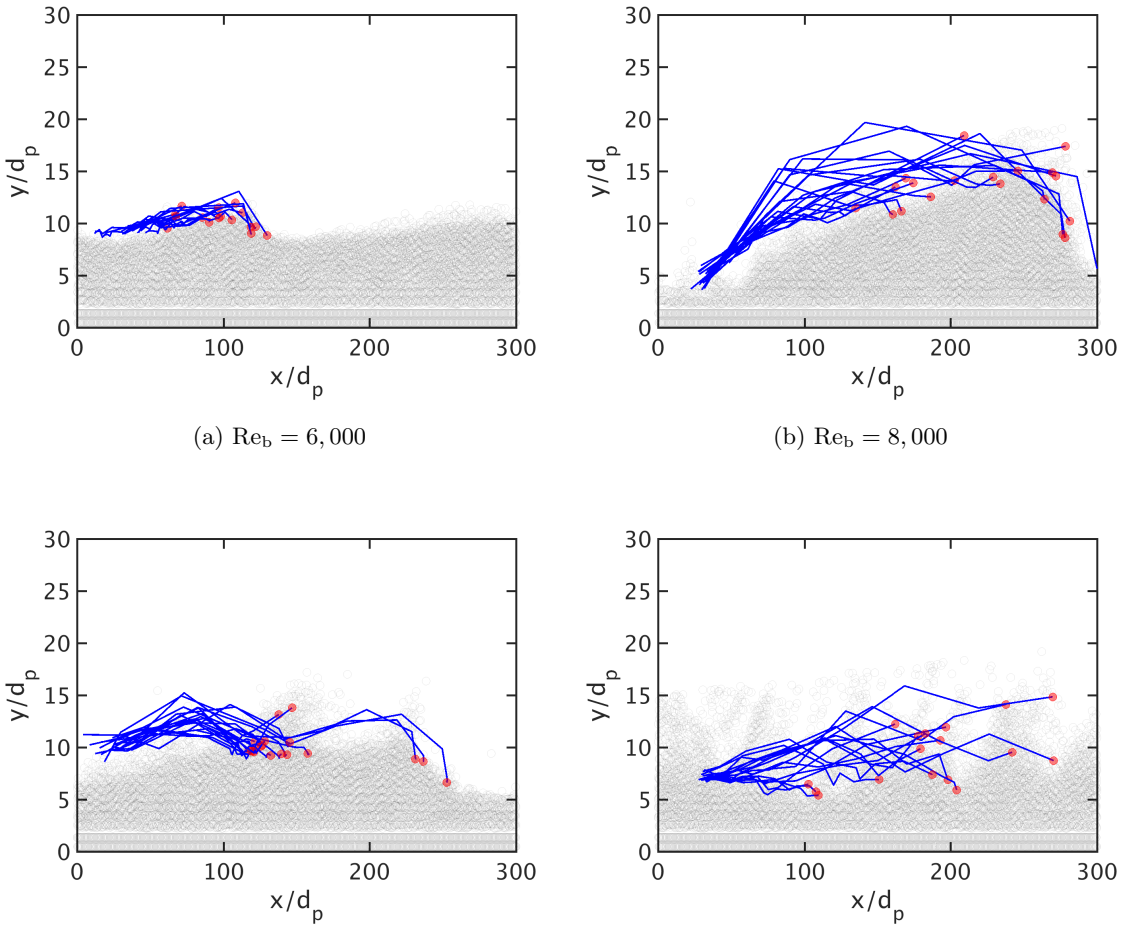

(a) $\mathrm{Re_b} = 6,000$

(b) $\mathrm{Re_b} = 8,000$

(c) $\mathrm{Re_b} = 10,000$

(d) $\mathrm{Re_b} = 12,000$

Figure 6: Comparison of the trajectories of the sediment particles on the crest of the dune during $t^* \in [700, 725]$ at different bulk Reynolds numbers. Each circle represents a sphere particle: red circle are highlighted particles; gray particles are non-highlighted. Solid lines are the trajectories of the highlighted particles.

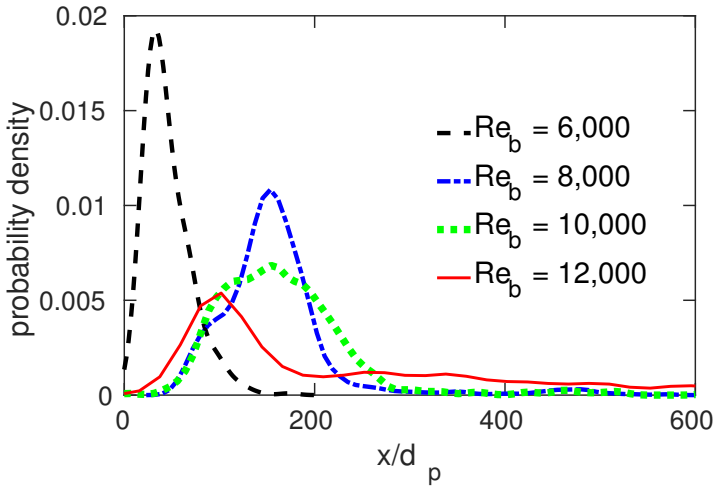

Figure 7: Comparison of the probability density functions of the longitudinal jumping length of the sediment particles during $t^* \in [700, 725]$.

exposed on the dune surface because of flow erosion on the stoss side. Once the previous buried particles are exposed on the dune surface, they can be entrained in the fluid flow and move on the surface of the dune.

5.4. Averaged sediment transport characteristics

In addition to the characteristics of individual sediment particles, the averaged quantities of sediment particles are detailed to investigate their spacial variation due to dune generation and migration. In this section, the sediment concentration, the sediment velocity, the particle entrainment and deposition rates, and the bed and suspended loads are investigated. These quantities are averaged both in time and laterally in a moving frame of reference to present the quantities as a function of the vertical direction, z, and the relative longitudinal location $X = x - U_d t$ with respect to the dune.

The contours of the moving-averaged sediment concentration and velocity from $t^* \in [600, 800]$ are shown in Fig. 9. This demonstrates the variation of sediment concentration and velocity at different bulk Reynolds numbers and sediment transport regimes. It can be seen in the concentration contours that the sediment concentration is more diffusive at larger Reynolds numbers. At $\mathrm{Re_b} = 6{,}000$, the dune migration velocity is stable, and the distance δ_s between the concentration isosurfaces of $\varepsilon_s = 0.1$ and 0.5 is $2d_p$. At $\mathrm{Re_b} = 8{,}000$, although the dune migration velocity is

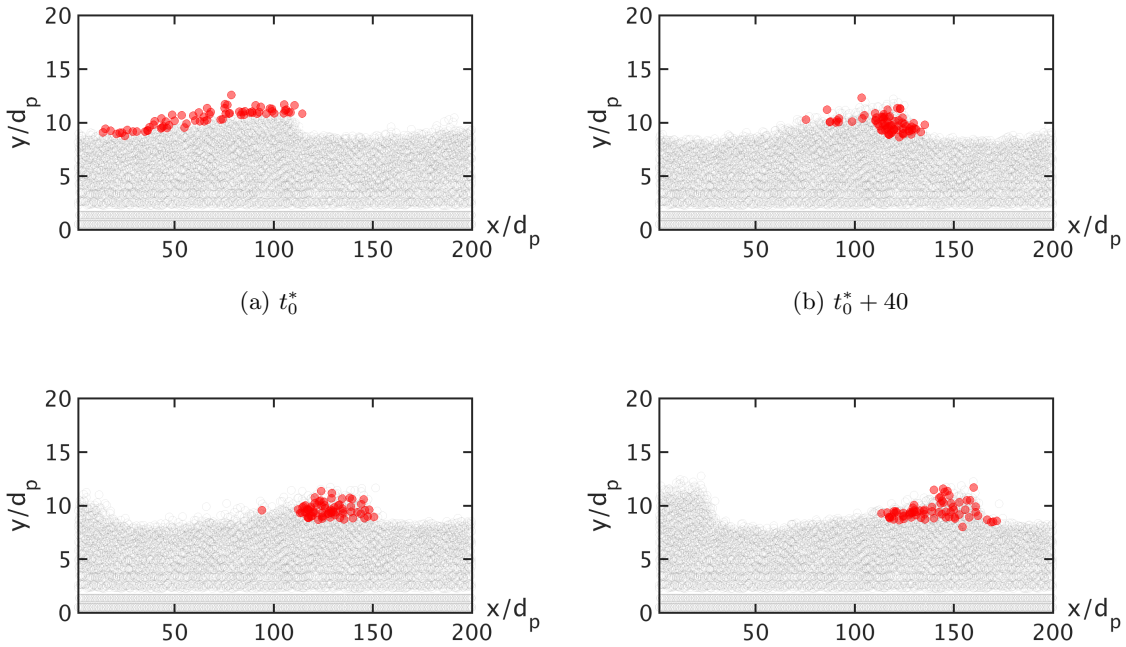

(a) t_0^* (b) $t_0^* + 40$

(c) $t_0^* + 80$ (d) $t_0^* + 120$

Figure 8: The snapshots of the burial of the sediment particles on the crest of the dune at bulk Reynolds number $\mathrm{Re_b} = 6{,}000$. Each circle represents a sphere particle: red circle are highlighted particles; gray particles are non-highlighted. The first snapshot corresponds to non-dimensional time $t_0^* = 700$.

stable, the saltation height of the sand particle is increased, and thus the distance δ_s increases. When the bulk Reynolds number increases to 12,000, the suspended load becomes dominant, and there is a dramatic increase in the momentum exchange between the fluid and sediment particle. Therefore, the distance between the concentration isosurfaces δ_s can be as large as $10d_p$. It should be noted that the dune-like features in Figs. 9(c) and 9(d) is because of the generation of unstable dunes. Moreover, the magnitude and direction of particle velocity are plotted using arrows on top of the concentration contour. This aims to demonstrate the averaged motion of sand particles and its correlation to dune surface. It can be seen in both Fig. 9(a) and 9(b) that the particle velocity at the crest of both dunes are larger than at other locations. This is due to the increase of the fluid velocity at the dune crest, which is also consistent with the findings in previous experimental measurements (*Kostaschuk et al.*, 2004, 2009). The dune height at $\mathrm{Re_b} = 8{,}000$ is larger than that at $\mathrm{Re_b} = 6{,}000$, and the vertical component of the particle velocity is also larger. The arrows of the particle velocity under the dune is too small and are not visible in the figure. This can be explained by the fact that the influence of fluid flow on the sediment particles is small in regions with higher sediment concentrations.

In the vertical direction, the quantities of interest to study sediment transport are the sediment entrainment and deposition, which are difficult to measure directly in experiments. Here we present both entrainment rate q_e and deposition rate q_d, which are a product of average sediment concentration and particle velocity $\varepsilon_s u_{p,y}$, i.e., they are the volume flux of sand particles per unit area. Since the behavior of individual particles can be traced, the entrainment rate is calculated using particles having positive vertical velocity; whereas the deposition rate is obtained by using particles having negative vertical velocity. The entrainment rate is plotted in Fig. 10. It should be noted that the entrainment rate is not constant along the vertical or streamwise directions. Therefore the sediment entrainment rates shown in the figure are a dune-averaged rate. The markers in the figure are the entrainment rates at $\varepsilon_s = 0.1$, and the error bars denote the range of the entrainment rates between the isosurfaces of sediment concentration $\varepsilon_s = 0.05$ to 0.5. Empirical functions for entrainment based on flume data are also shown in the figure (*Luque*, 1974; *van Rijn*, 1984c; *Emadzadeh and Cheng*, 2016). In general, the dune-averaged LES–DEM derived values fall within the range of these empirical formulas and are closest in value to that of *van Rijn* (1984c).

To demonstrate the variation of the vertical sediment transport, the entrainment rate and

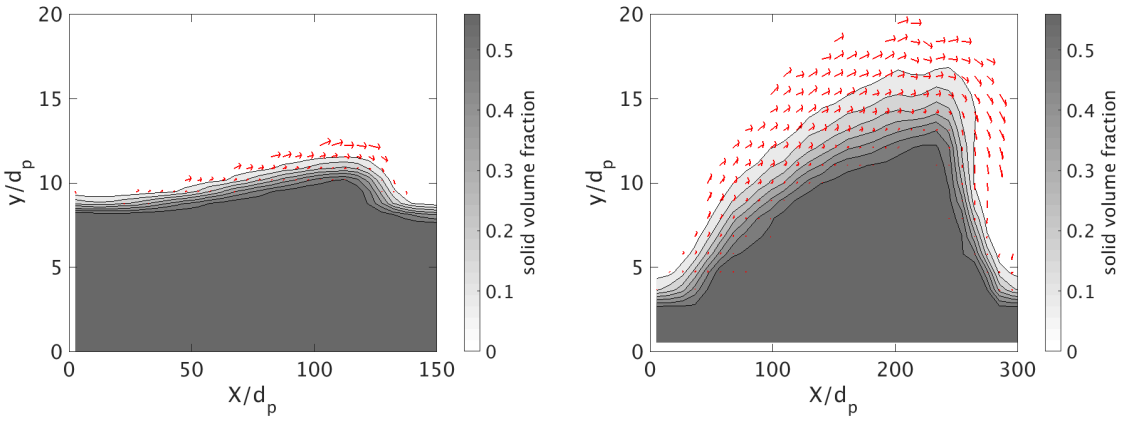

(a) Case 1: Re_b = 6,000

(b) Case 2: Re_b = 8,000

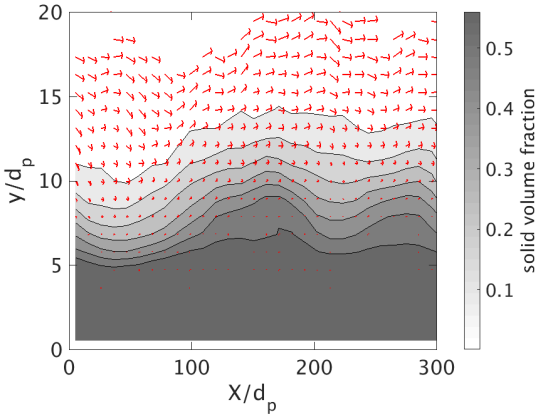

(c) Case 3: Re_b = 10,000

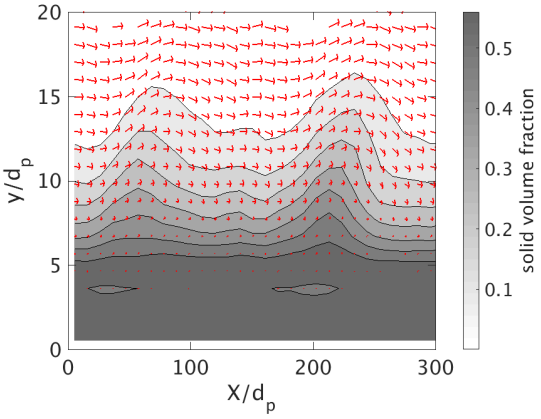

(d) Case 4: Re_b = 12,000

Figure 9: Moving-frame averaged solid concentration contour at various Reynolds nunmbers. On top of the concentration contour, the arrows denote the moving-frame averaged velocity of sediment particle.

deposition rate at the dune surface, $\varepsilon_s = 0.1$, are plotted as a function of the streamwise coordinate in Fig. 11. When the dune is stable in the moving frame of reference ($\mathrm{Re_b}$ = 6,000 and 8,000), the total sediment flux in the vertical direction is above zero on the stoss side of the dune, and becomes negative on the lee side. That is not to say that only entrainment occurs on the stoss and deposition in the wake, but rather that there is net entrainment over the stoss and net deposition in the wake. Both entrainment and deposition rate increase with Reynolds number.

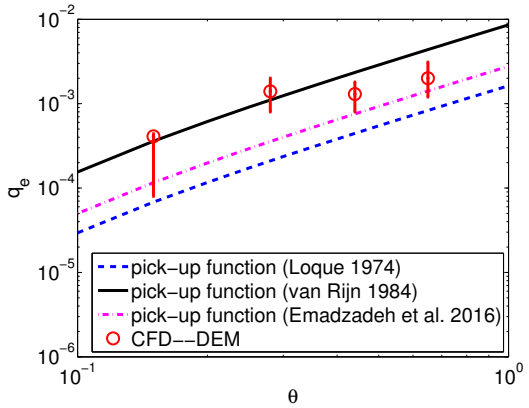

Figure 10: Horizontally averaged sediment entrainment rate during $t^* \in [700, 750]$ plotted as a function of Shields parameter. The markers indicate the entrainment rate obtained on the isosurface of $\varepsilon_s = 0.1$, and the error bars indicate the range of entrainment rates obtained at different isosurfaces ranging from $\varepsilon_s \in [0.05, 0.5]$.

In general, the total streamwise sediment transport rate, q_t or $q_t^* = q_t/d_p\sqrt{gR_sd_p}$ [-], can be found by integrating the particle velocities and concentrations over the total thickness of the domain and then averaging this over the length of the domain. These values are given in Table 2. However, it is also of interest to decompose this total downstream transport rate into bed, q_b, and suspended, q_s, load fractions. To do so, particles moving at $u_{p,x} > 3w_s$ are considered as suspended particles and those moving at $u_{p,x} \leq 3w_s$ are considered as bed load. $u_{p,x} = 3w_s$ is chosen as the distinguishing criteria between bed and suspended load because previous LES–DEM simulations of bed load transport have identified $u_{p,x} = 3w_s$ as the maximum velocity that a particle traveling in contact with the bed can attain (*Schmeeckle*, 2014; *Sun and Xiao*, 2016b). Based on these criteria, the simulations show an increase in the overall suspended load fraction, $\alpha_s = q_s/q_t$, from 0.06 in Case 1, up to $\alpha_s \approx 1$ at Case 4. Values for α_s are given in Table 2. Note that the total

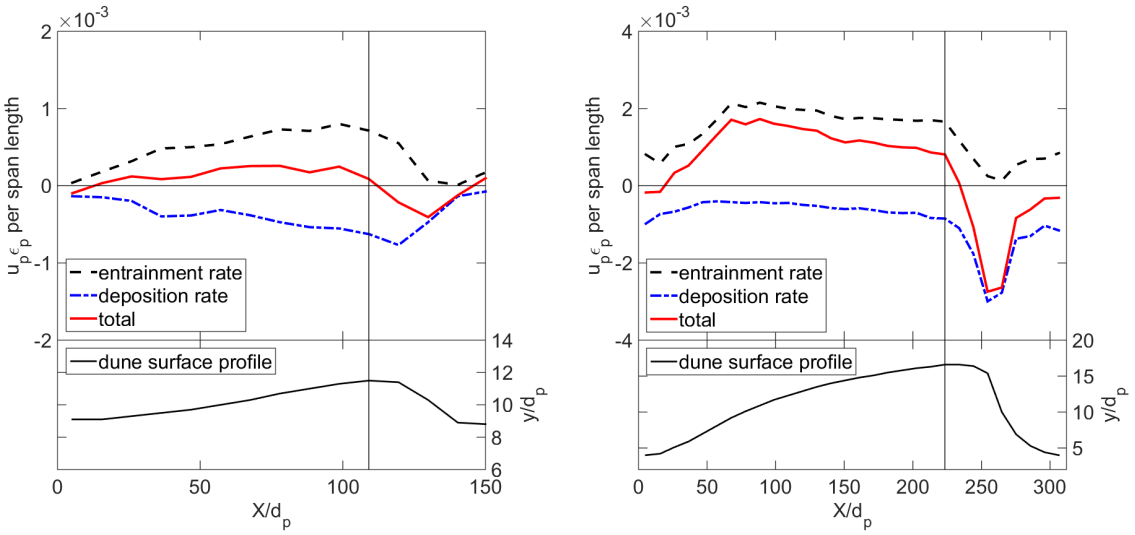

(a) Case 1: $\mathrm{Re_b} = 6{,}000$

(b) Case 2: $\mathrm{Re_b} = 8{,}000$

Figure 11: Comparison between the entrainment and deposition of sediment particles at $\mathrm{Re_b} = 6{,}000$ and 8,000. The vertical solid line in the figure indicates the location of the peak of the dune. The range of the x-axis in each panel is consistent with the dune wavelength.

domain-averaged transport rates were used in the calculation of α_s.

We can also look at the distribution of the non-dimensional total, bed, and suspended loads over the length of a dune in a moving frame of reference. Such distributions are shown in Fig. 12 for Case 1 and 2. The most striking feature of the load distribution is that q_t^* follows the general shape of the dune. Total transport rates increase moving from the preceding trough up and over the dune stoss. Peak transport is reached near the crest of the dune and then rapidly falls off in the wake. At $\mathrm{Re_b} = 6{,}000$, bed load is by far the dominant contributor to the total transport rate. Additionally, no transport occurs in the trough between sequent dunes. That is, all sediment being transported in the domain is tied up in the movement of the dunes. However, at $\mathrm{Re_b} = 8{,}000$, a far greater percentage of the sediment being moved travels in suspension. Interestingly, the bed load transport rate at $\mathrm{Re_b} = 8{,}000$ is fairly constant in the streamwise direction over the length of the stoss. The peaking nature of the total transport rate over the length of the dune, therefore, comes from the increasing contribution of suspended load over the stoss as the particle velocities increase. As with the $\mathrm{Re_b} = 6{,}000$ case, bed load transport in the trough between sequent dunes goes to zero. However, the total transport rate remains positive in the trough due to the bypass contributions from suspended load (Fig. 12).

One additional way to estimate bed load transport rates is through use of the bedform height, celerity, and porosity (e.g., *Simons et al.*, 1965; *McElroy and Mohrig*, 2009). We calculated the bedform transport rate, q_{bf}, as:

$$q_{bf} = (1 - \phi) U_d \frac{H_d}{2} \tag{10}$$

where ϕ is the average porosity of the bed (taken to be $\phi = 0.5$); note Eq. (10) assumes the beforms are triangular in shape. Non-dimensional values of q_{bf} are given in Table 2 for Cases 1 and 2 using values of U_d and H_d also reported in the same table. Eq. (10) did well in estimating the total transport load in Case 1 ($\mathrm{Re_b}$= 6,000); $q_{bf}^* = 0.06$ compared to $q_t^* = 0.05$. This result is reasonable seeing that the total transport rates go to zero in the dune troughs for Case 1 (Fig. 12(a)). The value of $q_{bf}^* = 0.93$ in Case 2 is larger than that in Case 1, but is smaller than the total load determined from the particle motions, $q_t^* = 1.12$. The reduction in q_{bf} relative to q_t^* is likely an outcome of the fact that q_t^* does not go to zero in the trough for the $\mathrm{Re_b}$= 8,000 run (Fig. 12(b)). Interestingly, while q_{bf}^* was smaller than the total load at this condition, q_{bf}^* was higher than the bed load transport rate, $q_b^* = 0.52$. This implies that some of the material counted as suspended load, in

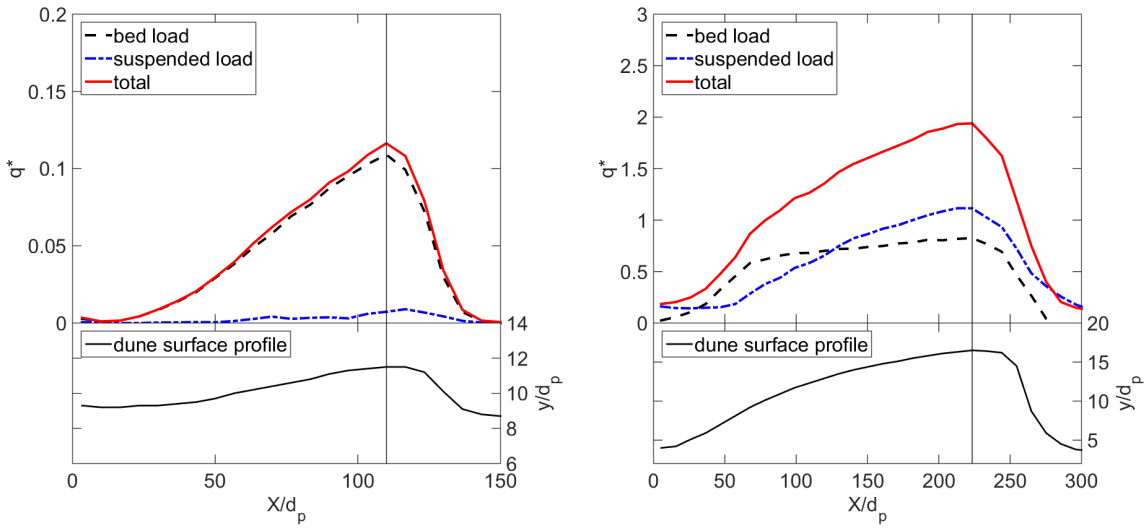

(a) Case 1: $\mathrm{Re_b} = 6{,}000$

(b) Case 2: $\mathrm{Re_b} = 8{,}000$

Figure 12: Comparison between the bed load and suspended load of sediment particles at bulk Reynolds number $\mathrm{Re_b} = 6{,}000$ and 8,000. The vertical line in the figure indicates the location of the peak of the dune. The range of the x-axis in each panel is consistent with the dune wavelength.

our definition of suspended load, was contributing to the migration of the bedform. Assuming that the suspended load can be determined from a difference between the total load and dune transport rate, $q_s^* = q_t^* - q_{bf}^*$, yields a suspended load fraction at $\mathrm{Re_b}$= 8,000 of $\alpha_s = 0.17$; which is less than half of the of α_s value determined using our definition of suspended load as $u_p > 3w_s$.

The thickness of both the bed and suspended load layers are shown as a function of the streamwise coordinate in Fig. 13. The height of the bed load layer is defined as the distance of the isosurfaces of sediment concentrations ε_s between 0.1 and 0.5, and the height of suspended load layer is the distance of the concentration isosurfaces between 0.02 and 0.1. The dune surface profiles are also plotted to help illustrate the location of peaks of the thickness. It can be seen in Fig. 13 that the maximum heights of both bed and suspended load layers are not at the peak of the dune but on the lee side of the dune. The increase of the bed load layer thickness is because the slope of the dune on the lee side is significantly larger than the stoss side, and the thickness in the vertical direction increases due to the increase of the slope; whereas the increase of suspended load layer thickness at $\mathrm{Re_b}$ = 8,000 is due to particle suspension in the recirculation region after the dune peak. It can be also seen in the figure that both the thickness of the bed load layer and suspended load layer is increasing when the bulk Reynolds number increases. The moving-frame averaged particle velocity is also plotted as a function of streamwise coordinate in Fig. 13. It can be seen in the figure that the trend of average particle velocity is consistent with the dune profiles, which is consistent with the trend of sediment transport rate in Fig. 12.

6. Discussion and Conclusion

In this study, we have investigated the individual particle motions associated with self-generated dunes at different bulk Reynolds numbers, or transport stages, using *SediFoam*. The simulations presented cover a range of transport conditions from bedform inception at transport stage of $\theta/\theta_{cr} = 4.6$ to washout conditions (at approximately $\theta/\theta_{cr} > 10$ and $w_s/u'_* \approx 1$). Calculation of the individual particle statistics showed that washout starts to occur when the jump length of the individual particle starts to exceed the wavelength of the dune and computational domain. This also coincided with a transition from bed load dominated transport to suspended load dominated transport.

When dunes were present, both bed and suspended load increased over the stoss side of the

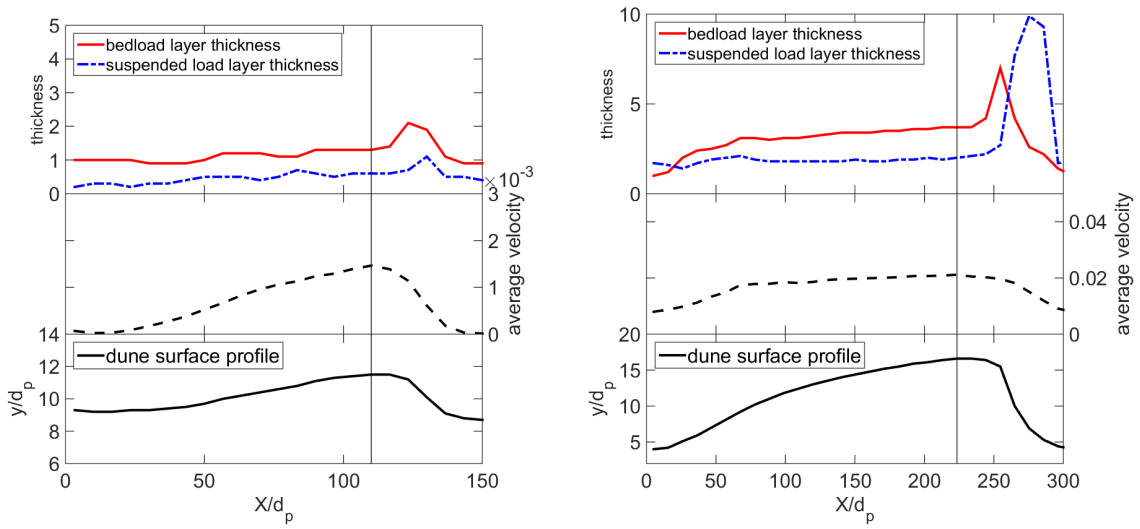

(a) Case 1: $\mathrm{Re_b} = 6{,}000$

(b) Case 2: $\mathrm{Re_b} = 8{,}000$

Figure 13: Comparison between the thickness of bed load/suspended load layer and sediment particle velocity at $\mathrm{Re_b} = 6{,}000$ and 8,000. The range of the x-axis in each panel is consistent with the dune wavelength.

dune; reaching a peak in the individual particle and total transport just at or before the crest of the dune. For the lower transport conditions ($\theta/\theta_{cr} = 4.6$ and $w_s/u'_* = 1.88$), material moved almost exclusively in bed load, and nearly 100% of the material transported from and over the stoss was trapped in the lee-side wake. No material bypassed the dune. At this condition, the total sediment transport rate was well approximated by the bedform transport rate calculated using the dune height, celerity, and bed porosity (Eq. (10)). As contributions from suspended load increased ($\theta/\theta_{cr} = 8.5$ and $w_s/u'_* = 1.33$), a fraction of the sediment was found to bypass the dune trough. This resulted in a positive sediment transport rate through the dune trough. One result of this was that the transport rate predicted from the bedform properties underestimated the total transport rate. In this case, the difference between the total load and sediment transport rate associated with dune migration was not equal to the suspended load transport rate. In our definition of suspended load, material can be picked up in suspension and deposited back down onto the dune in a way that contributes to the overall size and migration speed of the dune. Hence, calculating the transport rate from the dune properties included contributions from both bed and suspended load.

In this study we do not examine the fluid mechanics of the system or the links between coherent flow and the sediment motion. Instead, we have highlighted the ability of LES–DEM methods to obtain the detailed particle motion data that cannot, at least as of yet, be obtained through field or laboratory studies of sand beds. The type and amount of data that can be generated with such methods is rather staggering, and the presence of mobile bedforms presents added challenges with regard to presenting the detailed data in a meaningful way. In this paper, we have chosen to present data on individual particle jump lengths, particle entrainment into suspension, and the fractionation between bed and suspended load within a moving frame of reference that is tied to the celerity of the bedforms. We demonstrate that the LES–DEM method can be used to both investigate individual particle dynamics and extract key sediment transport quantities needed to bolster modeling of mobile beds in coarser resolution simulations. For example, use of the LES–DEM method allowed for the evaluation of the particle pickup rates over the heterogeneous stress field of the mobile dune surfaces. Depending on how the bed load and suspended load layers are conceptualized as existing, one could use this type of information to further develop models of suspended load entrainment under a range of condition.

While methods such as *SediFoam* are opening up new doors for the exploration of detailed

particle dynamics in sediment transport research, such simulations are still limited by computational resources. For example, we were not able to generate stable bedforms at $\mathrm{Re_b} > 8,000$ (or $\theta/\theta_{cr} > 10$). At this point it is difficult to say whether the dunes were washed out because the mode of transport switched unequivocally to suspended load or because the domain became smaller than the jump length of the particles. For example, at $\mathrm{Re_b}$ =10,000 and 12,000, correlated waves of suspended load could be observed moving through the domain (Figs. 9(c) and 9(d)). Perhaps such waves would lead to longer wavelength bedforms given enough space. However, doubling the size of the domain would further increase the number of particles and the mesh size required to resolve the flow field, leading to increased computational costs. Another avenue left to push towards in the application of LES–DEM methods for sand bed research is the incorporation of deeper flows, the presence of a free surface, and the use of a grain size distribution within the bed. As such advances come to fruition, it is possible to conceive of parametric numerical simulations being run to better refine our understanding of the particle physics involved in the movement of sand through rivers.

7. Acknowledgments

The computational resources used for this project are provided by the Advanced Research Computing (ARC) of Virginia Tech, which is gratefully acknowledged. RS gratefully acknowledges partial funding of graduate research assistantship from the Institute for Critical Technology and Applied Science (ICTAS, grant number 175258) in this effort. To access data used in this paper, please contact the corresponding author.

References

Ancey, C. (2010), Stochastic modeling in sediment dynamics: Exner equation for planar bed incipient bed load transport conditions, *Journal of Geophysical Research*, *115*, F00A11.

Anderson, A. (1953), The characteristics of sediment waves formed by flow in open channels, in *Proc. Third Mid- Western Conf. on Fluid Mech.*, pp. 379–395, University of Minnesota.

Anderson, T., and R. Jackson (1967), A fluid mechanical description of fluidized beds: Equations of motion, *Industrial and Chemistry Engineering Fundamentals*, *6*, 527–534.

Arolla, S. K., and O. Desjardins (2015), Transport modeling of sedimenting particles in a turbulent pipe flow using Euler–Lagrange large eddy simulation, *International Journal of Multiphase Flow*, *75*, 1 – 11.

Aussillous, P., J. Chauchat, M. Pailha, M. Médale, and É. Guazzelli (2013), Investigation of the mobile granular layer in bedload transport by laminar shearing flows, *Journal of Fluid Mechanics*, *736*, 594–615.

Best, J. (2005), The fluid dynamics of river dunes: A review and some future research directions, *Journal of Geophysical Research: Earth Surface (2003–2012)*, *110*, F04S02.

Campagnol, J., A. Radice, F. Ballio, and V. Nikora (2015), Particle motion and diffusion at weak bed load: accounting for unsteadiness effects of entrainment and disentrainment, *Journal of Hydraulic Research*, *53*(5), 633–648.

Charru, F., B. Andreotti, and P. Claudin (2013), Sand ripples and dunes, *Annual Review of Fluid Mechanics*, *45*(1), 469–493.

Cundall, P., and D. Strack (1979), A discrete numerical model for granular assemblies, *Géotechnique*, *29*, 47–65.

Ebrahimi, M. (2014), CFD–DEM modelling of two-phase pneumatic conveying with experimental validation., Ph.D. thesis.

Emadzadeh, A., and N.-S. Cheng (2016), Measurements of sediment pickup rate over dune-covered bed, *Environmental Fluid Mechanics*, *16*(1), 123–144.

Fathel, S. L., D. J. Furbish, and M. W. Schmeeckle (2015), Experimental evidence of statistical ensemble behavior in bed load sediment transport, *Journal of Geophysical Research: Earth Surface*, *120*(11), 2298–2317.

Fukuoka, S., T. Fukuda, and T. Uchida (2014), Effects of sizes and shapes of gravel particles on sediment transports and bed variations in a numerical movable-bed channel, *Advances in Water Resources*, *72*, 84 – 96.

Furbish, D. J., P. K. Haff, J. C. Roseberry, and M. W. Schmeeckle (2012), A probabilistic description of the bed load sediment flux: 1. Theory, *Journal of Geophysical Research: Earth Surface*, *117*(F3).

Furbish, D. J., M. W. Schmeeckle, R. Schumer, and S. L. Fathel (2016), Probability distributions of bed-load particle velocities, accelerations, hop distances and travel times informed by Jaynes's principle of maximum entropy, *Journal of Geophysical Research: Earth Surface*, *121*(7), 1373–1390.

Garcia, M., and G. Parker (1991), Entrainment of bed sediment into suspension, *Journal of Hydraulic Engineering*, *117*(4), 414–435.

García, M. H. (2008), *Sediment Transport and Morphodynamics. Sedimentation Engineering*, chap. 2 Sediment Transport and Morphodynamics, pp. 21–163, ASCE Manuals and Reports on Engineering Practice No. 110, ASCE.

García, M. H., E. M. Laursen, C. Michel, and J. M. Buffington (2000), The legend of A. F. Shields, *Journal of Hydraulic Engineering*, *126*(9), 718–723.

Gilbert, G. K. (1914), The transportation of debris by running water, *Professional Papers 86*, U.S. Geological Survey.

Goniva, C., C. Kloss, and S. Pirker (2009), Towards fast parallel CFD–DEM: an open-source perspective, in *Proc. of Open Source CFD International Conference*.

Guy, H. P., D. B. Simons, and E. V. Richardson (1966), Summary of alluvial channel data from flume experiments, 1956-61, *USGS Professional Paper 462-I*.

Han, T., A. Levy, and H. Kalman (2003), DEM simulation for attrition of salt during dilute-phase pneumatic conveying, *Powder Technology*, *129*(1), 92–100.

Horiuti, K. (1985), Large eddy simulation of turbulent channel flow by one-equation modeling, *Journal of the Physical Society of Japan*, *54*(8), 2855–2865.

Issa, R. I. (1986), Solution of the implicitly discretised fluid flow equations by operator-splitting, *Journal of Computational Physics*, *62*(1), 40–65.

Jasak, H. (1996), Error analysis and estimation for the finite volume method with applications to fluid flows, Ph.D. thesis, Imperial College London (University of London).

Kafui, K., C. Thornton, and M. Adams (2002), Discrete particle–continuum fluid modelling of gas–solid fluidised beds, *Chemical Engineering Science*, *57*(13).

Kempe, T., B. Vowinckel, and J. Fröhlich (2014), On the relevance of collision modeling for interface-resolving simulations of sediment transport in open channel flow, *International Journal of Multiphase Flow*, *58*, 214 – 235.

Kennedy, J. (1963), The mechanics of dunes and antidunes in erodible-bed channels, *Journal of Fluid Mechanics*, *16*(4), 521–544.

Kidanemariam, A. G., and M. Uhlmann (2014), Direct numerical simulation of pattern formation in subaqueous sediment, *Journal of Fluid Mechanics*, *750*(R2), 1–13.

Kloss, C., C. Goniva, A. Hager, S. Amberger, and S. Pirker (2012), Models, algorithms and validation for opensource DEM and CFD–DEM, *Progress in Computational Fluid Dynamics, an International Journal*, *12*(2), 140–152.

Kostaschuk, R., P. Villard, and J. Best (2004), Measuring velocity and shear stress over dunes with acoustic doppler profiler, *Journal of hydraulic engineering*, *130*(9), 932–936.

Kostaschuk, R., D. Shugar, J. Best, D. Parsons, S. Lane, R. Hardy, and O. Orfeo (2009), Suspended sediment transport and deposition over a dune: Río paraná, argentina, *Earth Surface Processes and Landforms*, *34*(12), 1605–1611.

Lajeunesse, E., L. Malverti, and F. Charru (2010), Bed load transport in turbulent flow at the grain scale: Experiments and modeling, *Journal of Geophysical Research*, *115*(F4), F04,001.

Luque, R. F. (1974), Erosion and transport of bed-load sediment, Ph.D. thesis, TU Delft, Delft University of Technology.

McElroy, B., and D. Mohrig (2009), Nature of deformation of sandy bed forms, *Journal of Geophysical Research: Earth Surface*, *114*(F3).

Mohrig, D., and J. D. Smith (1996), Predicting the migration rates of subaqueous dunes, *Water Resources Research*, *32*(10), 3207–3217.

Naqshband, S., J. S. Ribberink, D. Hurther, and S. J. M. H. Hulscher (2014), Bed load and suspended load contributions to migrating sand dunes in equilibrium, *Journal of Geophysical Research: Earth Surface*, *119*(5), 1043–1063.

OpenCFD (2013), *OpenFOAM User Guide*, see also `http://www.opencfd.co.uk/openfoam`.

Ouriemi, M., P. Aussillous, and E. Guazzelli (2009), Sediment dynamics. Part 2. Dune formation in pipe flow, *Journal of Fluid Mechanics*, *636*, 321–336.

Paarlberg, A., C. Dohmen-Janssen, S. Hulscher, J. Van den Berg, and A. Termes (2006), Modelling morphodynamic evolution of river dunes, in *Proceedings of the International Conference on Fluvial Hydraulics, 6–8 September 2006, Lisbon, Portugal*, pp. 969–978.

Parker, G., C. Paola, and S. Leclair (2000), Probabilistic Exner sediment continuity equation for mixtures with no active layer, *Journal of Hydraulic Engineering*, *126*(11), 818–826.

Plimpton, J. (1995), Fast parallel algorithms for short-range molecular dynamics, *J. Comp. Phys.*, *117*, 1–19.

Roseberry, J. C., M. W. Schmeeckle, and D. J. Furbish (2012), A probabilistic description of the bed load sediment flux: 2. particle activity and motions, *Journal of Geophysical Research: Earth Surface*, *117*, F03,032.

Saffman, P. (1965), The lift on a small sphere in a slow shear flow, *Journal of fluid mechanics*, *22*(02), 385–400.

Schmeeckle, M. W. (2014), Numerical simulation of turbulence and sediment transport of medium sand, *Journal of Geophysical Research: Earth Surface*, *119*, 1240–1262.

Simons, D. B., E. V. Richardson, and C. F. Nordin Jr. (1965), Bedload equation for ripples and dunes, *Tech. Rep. 462-H, 1-9*, U.S. Geological Survey Professional Papers.

Smith, J. D., and S. R. McLean (1977), Spatially averaged flow over a wavy surface, *Journal of Geophysical Research*, *82*(12), 1735–1746.

Sun, J., F. Battaglia, and S. Subramaniam (2007), Hybrid two-fluid DEM simulation of gas-solid fluidized beds, *Journal of Fluids Engineering*, *129*(11), 1394–1403.

Sun, R., and H. Xiao (2015a), Diffusion-based coarse graining in hybrid continuum–discrete solvers: Applications in CFD–DEM, *International Journal of Multiphase Flow*, *72*, 233–247.

Sun, R., and H. Xiao (2015b), Diffusion-based coarse graining in hybrid continuum–discrete solvers: Theoretical formulation and a priori tests, *International Journal of Multiphase Flow*, *77*, 142 – 157.

Sun, R., and H. Xiao (2016a), CFD–DEM simulations of current-induced dune formation and morphological evolution, *Advances in Water Resources*, *92*, 228–239.

Sun, R., and H. Xiao (2016b), SediFoam: A general-purpose, open-source CFD–DEM solver for particle-laden flow with emphasis on sediment transport, *Computers & Geosciences*, *89*, 207 – 219.

Syamlal, M., W. Rogers, and T. O'Brien (1993), MFIX documentation: Theory guide, *Tech. rep.*, National Energy Technology Laboratory, Department of Energy.

Tsuji, Y., T. Kawaguchi, and T. Tanaka (1993), Discrete particle simulation of two-dimensional fluidized bed, *Powder Technolgy*, *77*(79-87).

van Rijn, L. (1984a), Sediment transport, part I: Bed load transport, *Journal of hydraulic engineering*, *110*(10), 1431–1456.

van Rijn, L. C. (1984b), Sediment transport, part III: Bed forms and alluvial roughness, *Journal of Hydraulic Engineering*, *110*(12), 1733–1754.

van Rijn, L. C. (1984c), Sediment pick-up functions, *Journal of Hydraulic Engineering*, *110*(10), 1494–1502.

Venditti, J. G., C. M. Lin, and M. Kazemi (2016), Variability in bedform morphology and kinematics with transport stage, *Sedimentology*, *63*(4), 1017–1040.

Vowinckel, B., T. Kempe, and J. Fröhlich (2014), Fluid–particle interaction in turbulent open channel flow with fully-resolved mobile beds, *Advances in Water Resources*, *72*, 32 – 44.

Yoshizawa, A., and K. Horiuti (1985), A statistically-derived subgrid-scale kinetic energy model for the large-eddy simulation of turbulent flows, *Journal of the Physical Society of Japan*, *54*(8), 2834–2839.

Zhu, H., Z. Zhou, R. Yang, and A. Yu (2007), Discrete particle simulation of particulate systems: theoretical developments, *Chemical Engineering Science*, *62*(13), 3378–3396.